Proceedings World Geothermal Congress 2020+1
Reykjavik, Iceland, April - October 2021

Observation of Hydromechanical Fracture Movements During Stimulation of the EGS Basel Reservoir

Francisco Serbeto, Peter Meier

Geo-Energie Suisse. Reitergasse 11 8004 Zürich Switzerland

f.serbeto@geo-energie.ch, p.meier@geo-energie.ch

Keywords: Fractures, stimulation, hydraulic modelling.

ABSTRACT

During the first 100 hours of the Basel (Switzerland) stimulation, numerous sudden and sharp pressure drops (up to -1 MPa) and pressure build-ups (up to 1.7 MPa) concur with the timestamp of seismic events that are located close to the injection interval and that have generally stronger magnitudes of up to 1.7. After 100 hours, the effects of induced seismicity on pressures vanishes also for stronger magnitudes of up to 3.4. A 1D radial flow model that incorporates spatio-temporal variations of flow dimension (n), hydraulic conductivity (K) and storativity (S), can adequately reproduce the observed pressure and flow rate behavior of approximately 9 days of the stimulation including injection, shut-in and back-flow periods. In particular, the temporal variation of the flow dimension reveals different hydraulic regimes during and after injection, i.e., pseudo-radial flow during stimulation and channelized preferential flow during shut-in and backflow periods. The modelled pressure profile is in good agreement with the propagation of the observed seismic cloud. The pressures necessary for the propagation of the stimulation front are estimated to be in the order of 2 to 3 MPa. We conclude that basic hydraulic modelling can be used as a good approximation for the radial pressure distribution during stimulation of an EGS reservoir.

1. INTRODUCTION

The Basel Enhanced Geothermal System (EGS hereinafter) was drilled to a total depth of 5000 m with a 398.1 m openhole section. The reservoir was stimulated by injecting 11570 m^3 of water for 6 days, after which a short shut-in phase and a prolonged bleed-off of 3400 m^3 was done (Häring et al., 2008). During the bleed-off, a 3.4 magnitude seismic event associated with the injection was felt in the city of Basel, which finally led to the permanent suspension of the geothermal project.

The Basel project produced seismic and hydraulic data of exceptional quality. Generally, these data sets, especially the pressure transients, are used individually to estimate the mid-to-large scale properties of the reservoir by means of numerical modelling. For instance, the seismic catalogue was used to infer a plausible pressure field using purely mechanical models (Terakawa et al., 2012; Mukuhira et al., 2017; Terakawa, 2014). However, the available pressure curve was not fitted. Instead, Alcolea and Meier (2011) performed a conventional analysis of the pressure curve using deconvolution methods (Birsoy and Summers, 1980) and standard analytical solutions (Theis C. V., 1935) to fit the pressure curve. In that work, the extent of the seismic cloud was used to benchmark the extent of the predicted pressure cloud.

However, in the work mentioned above the interplay between seismic events and pressure fluctuations has not been recognized. In a recent review of the Basel data set we found during the first 100 hours of stimulation sharp and sudden pressure drops (up to -1MPa) and pressure build-ups (up to +1.7MPa) that are clearly associated with seismic events. Some of these pressure responses have been reported already by Ortiz et al. (2011) and were attributed to fracture propagation but not correlated with seismicity. In chapter 2 we present an analysis of the nature of these seismic events. In chapters 3 and 4 we show the results of calibrating an 1D radial numerical hydraulic model utilizing the spatial distribution of seismicity, borehole pressures and flow rates during injection, shut-in and backflow periods. The model includes only three hydraulic parameters, i.e., hydraulic conductivity, storativity and flow dimension, which vary both in space and time.

2. EVALUATION OF HYDRAULIC AND SEISMICITY DATA

We utilized the seismic catalogue of the Swiss seismological survey (SED) and the focal mechanism in Deichmann et al. (2014). The hydraulic data set consists of pressures at the well head and the flow rates, both measured every 60 seconds.

The uphole pressure curve is divided into three phases, i.e., injection ($t < 138.4$ h), shut-in (138.4 to 144.8 h) and bleed-off ($t > 144.8$ h). For convenience, the injection phase has been divided into early-time (first 16.6 h), mid-time (16.6 - 69.4 h), and late-time (69.4 to 138.4 h (shut-in)). The seismic catalogue contains 3321 hypocentre localizations and provides a representative set of events for statistics and modelling. To simplify the analysis, the event hypocentres have been projected to the best fit plane (154N 83N) of the whole seismic catalogue (Figure 1) and the distance of each hypocentre to the borehole have been calculated.

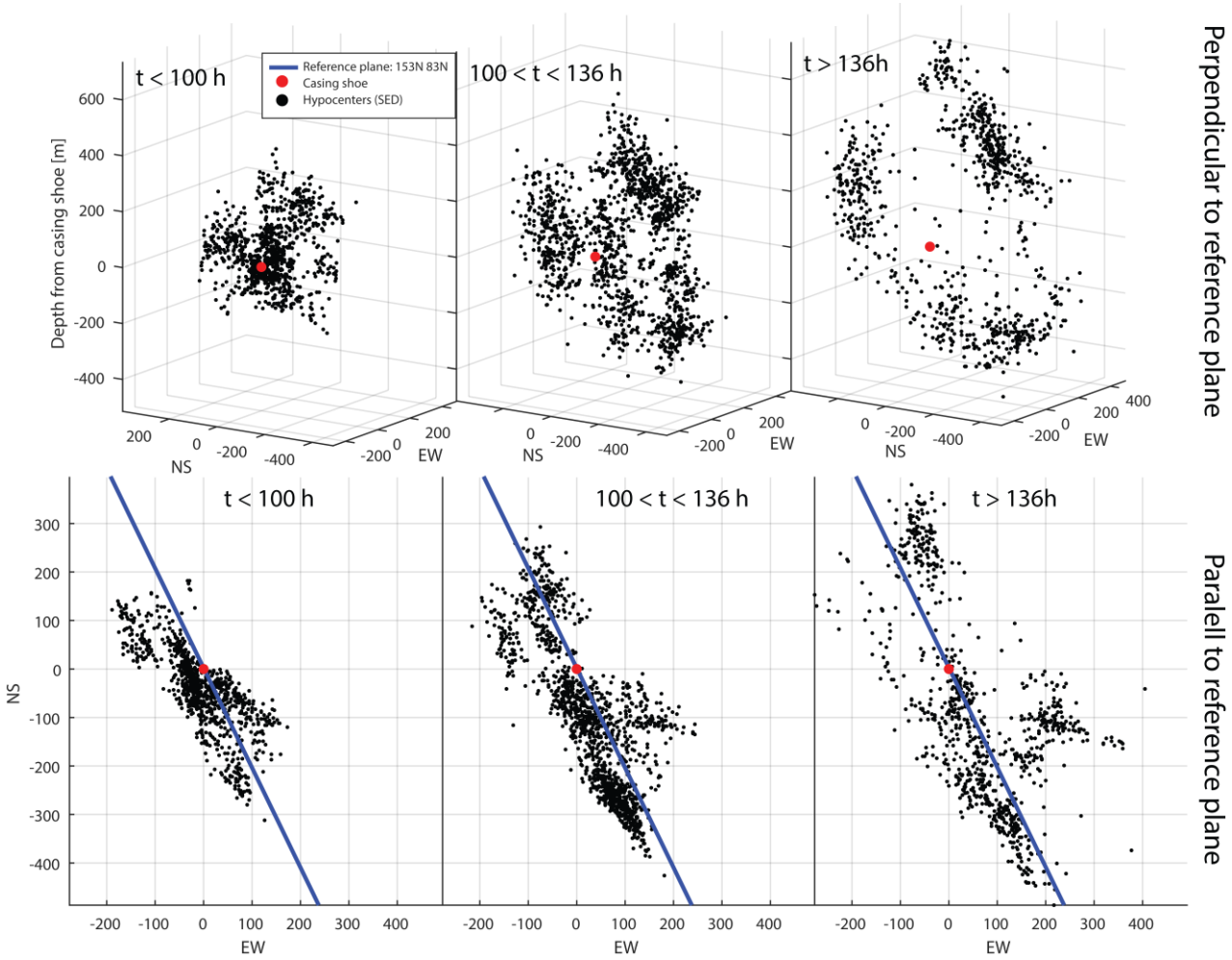

Figure 1: Extent of seismic cloud superimposed to the best fit reference plane. Top: Perpendicular to 154N 83N. Bottom: Parallel to plane (154N 83N).

The catalogue of focal mechanisms (Deichmann et al., 2014) contains 185 fault plane solutions and is used to understand the dominant mechanisms of hydro-shearing. The fault plane orientations derived from the focal mechanisms can be attributed to three dominant fracture plane sets observed at the borehole, which are: Set 1 (164N 70N), Set 2 (310N 56N) and Set 3 (121N 83S) which correspond to left lateral strike-slip, normal and right lateral strike-slip dominated, respectively (Serbeto and Meier, 2020).

During the injection phase, only the early-time (t < 16.6 h) and some of the mid-time (16.6 - 69.4 h) periods show concurrent timestamps of micro-seismic events and of pressure drops/build-ups of up to 1 MPa (Figures 2a and 2b). These variations dampen down in amplitude as the stimulation progresses. During the mid-time (16.6 - 69.4 h) period, two clear build-ups of up to 1.7 MPa are observed in the absence of flow rate variations (42.5 h and 55.4 h, red arrows in Figure 2b). No anomalous pressure variations were observed during the late time-period (69.4 h to shut-in). Effects of seismic events are probably masked by the frequent small fluctuations in both pressure and the flowrate curves (Figure 2c), which could be attributed to turbulent flow within fractures (Ortiz et. al, 2011). Anomalies are not observed during the shut-in and bleed-off phases regardless of the magnitude of the events or their distance to the borehole (Figure 2d), including the late time greater than magnitude 2 events and 3.4 event that ultimately led to the termination of the Basel project.

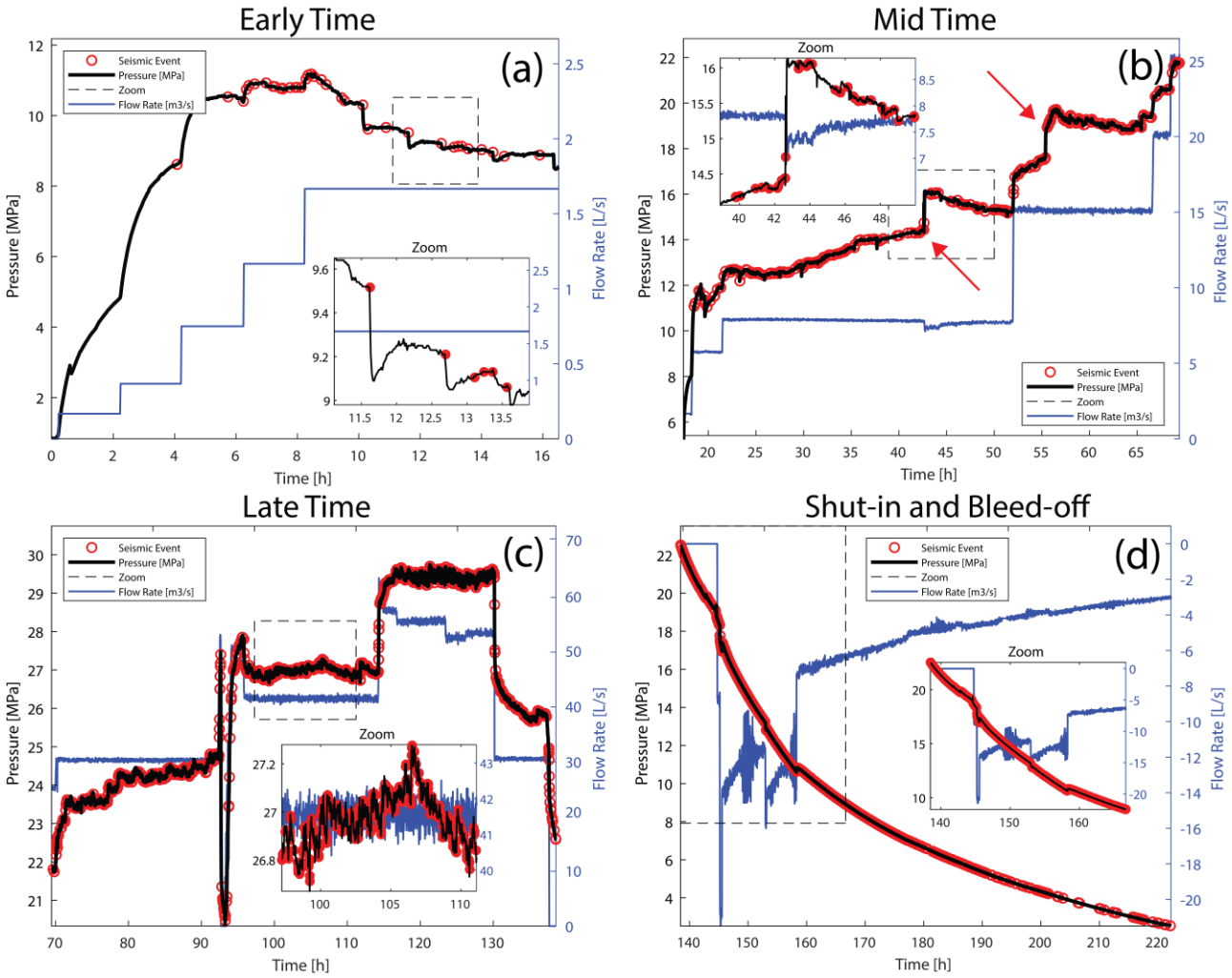

Figure 2: Time-concurrent pressure variations and induced micro-seismic events at Early times (a) and mid-times (b), the two red arrows show the two pressure increases of 1.7 MPa. At late times (c) and during shut-in and bleed-off (d), no effects of seismicity can be discerned on the pressure curves.

Micro-seismic events matching the timestamp of sharp pressure variations are analysed in terms of magnitude, distance to the borehole and the corresponding amplitude of the pressure variation. Figure 3a shows the correlation between event magnitude and amplitude of the pressure variation. As expected, larger event magnitudes (M>1) induce larger pressures variations and smaller pressure variations are caused by micro-seismic events far away from the borehole regardless of magnitude. Figure 3b displays the correlation between rupture mode and pressure variation. Set 1 and Set 2 events (left lateral strike-slip and normal faulting) lead generally to small pressure variations regardless of distance, except one event belonging to Set 2 (normal faulting) showing a strong pore pressure increases, possibly caused by local fracture closure. Finally, set 3 events (right lateral strike-slip) lead generally to negative pressure variations (i.e., pressure drops) except one event that produces a large pressure build-up of 1.27 MPa (Figure 3b, red arrow).

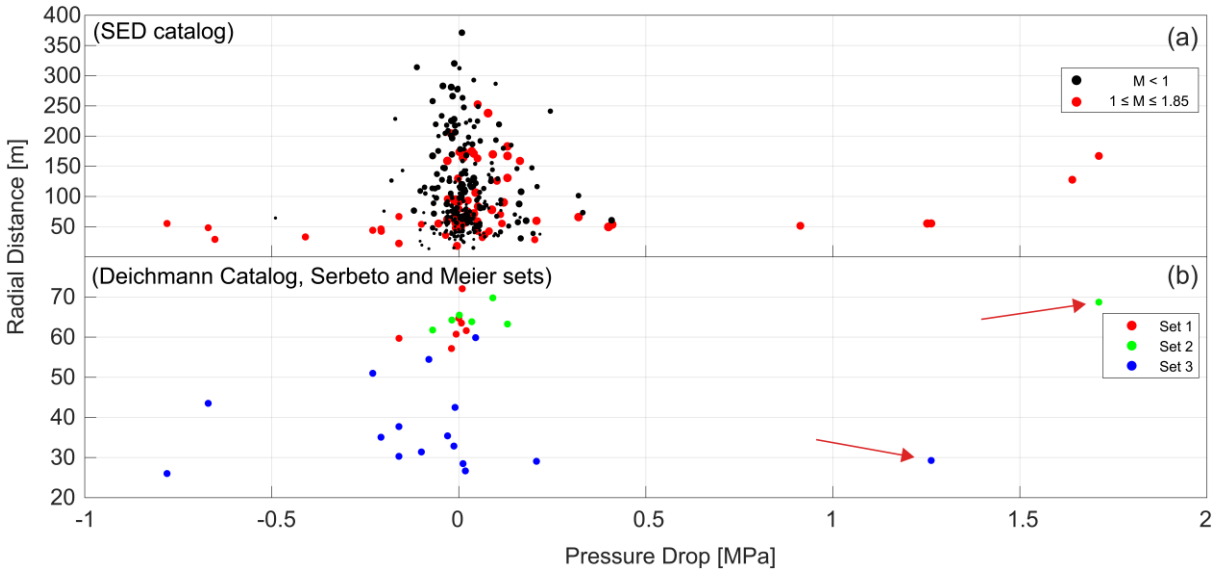

Figure 3: Pressure variations associated with seismic events. The vertical axis displays the distance between the hypocenter (circles) and the borehole. (a) Correlation between pressure change and event magnitude.; (b) Correlation between pressure drop and fracture sets in Serbeto and Meier (2020) derived from the focal mechanisms in Deichmann et al. (2014). The two pressure build-ups at 55.4 h and 42.5 h are marked with red arrows.

To acquire further insights on the hydromechanical fracture movements, the temporal evolution of the fault plane solution catalogue (Deichmann et al., 2014) was further analysed. Set 3 fracture planes are stimulated at the beginning (Figure 4c, 4d: clusters 14 and 15) and show shearing throughout the stimulation but with decreasing dominance (Figure 4d). Set 1 is the least dominant (Figure 4a), which is unexpected since this orientation constitutes 84% of the fractures detected by televiewer rendering (Ziegler et al., 2015). Finally, Set 2 is the most dominant fracture plane when the injection flow rate was decreased (130 h to 138.5 h) and during the shut-in (Figures 4b, 4d, periods 3a and 4).

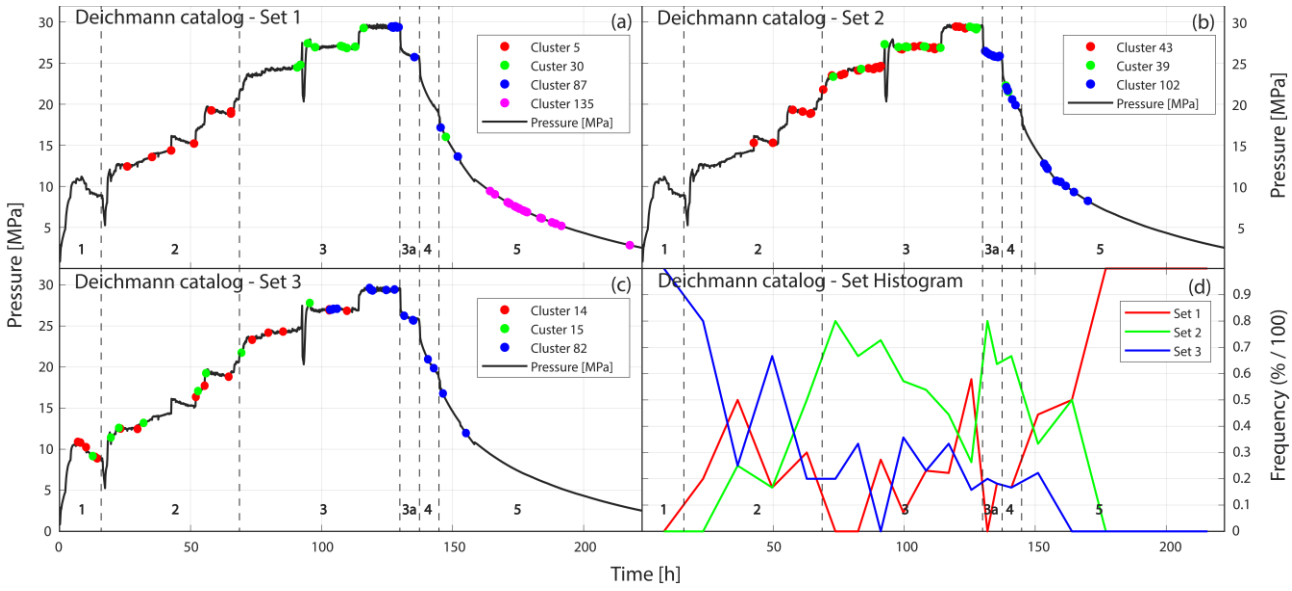

Figure 4: Temporal evolution of fault plane solution catalogue (Deichmann et al., 2014), categorized by the fracture set they belong to (Serbeto and Meier, 2020). a) Set 1, right lateral strike-slip. b) Set 2, normal faulting c) Set 3, left lateral strike-slip d) The proportion of each active set within each period. Time periods are marked with (1) for early-time, (2) for mid-time, (3) for late-time, (3a) for a part of late-time period in which the flowrate decreased, (4) for shut-in and (5) for bleed-off.

The histogram of distance of the seismic events from the borehole (Figure 5) shows that, at early times ($t < 100$ h), seismicity occurs near the borehole and decreases with radial distance. A bimodality appears between 100 h and the shut-in (136 h) where the seismicity near the borehole decreases and the maximum number of events has moved to 300 m. The bimodality suggests the existence of a highly stimulated zone of radius ≈200 m around the borehole where there is no substantial additional shearing. During the shut-in and back-flow phases ($t > 136$ h), the frequency of events up to ≈300 m from the borehole immediately drops but persists beyond ≈400 m suggesting that also at late times the dominant mechanism is radial propagation of the stimulated area.

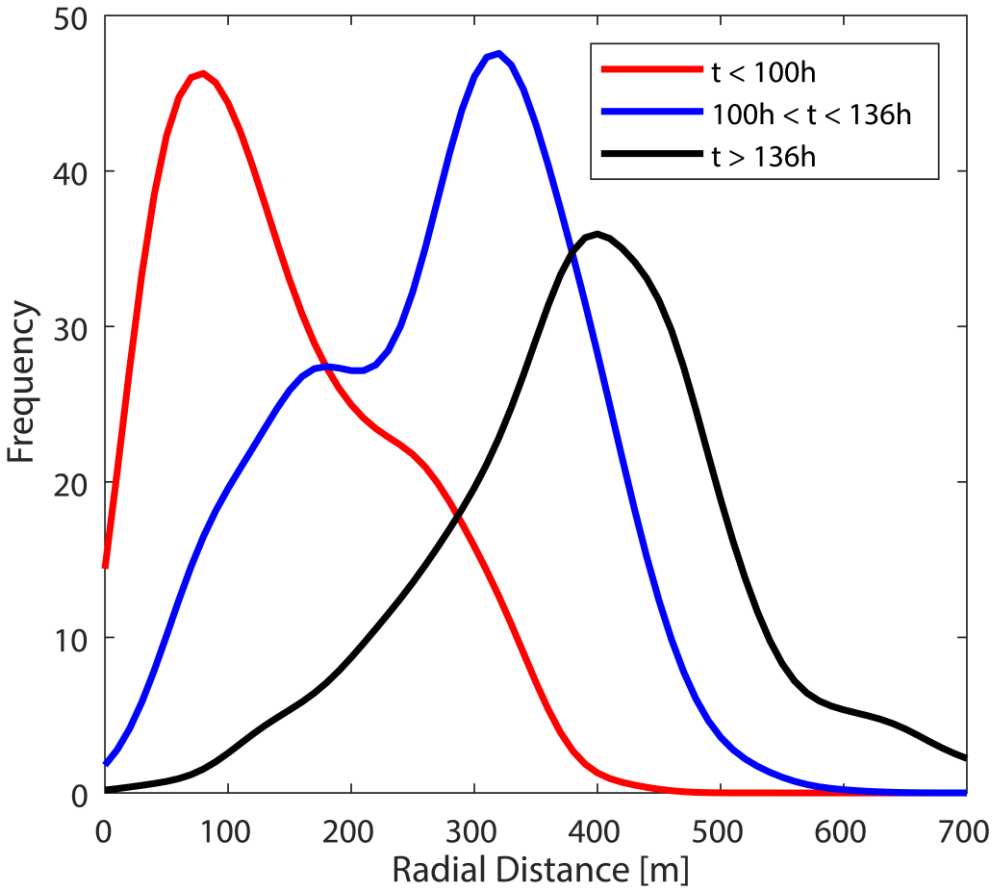

Figure 5: Histograms of seismic events as a function of radial distance from the borehole assuming a single projection plane N154 83N. The histogram bars have been replaced by a Kernel distribution to improve readability.

3. HYDRAULIC MODEL

So far, we have focused on the impact of seismicity at the closest vicinity of the borehole. However, equally interesting is the behavior of the system at large distances and the amount of correlation between the extent of the pressure and seismic cloud. To analyze that, we propose a radial hydraulic model built upon the conceptual model presented before. The main hydraulic properties, which vary in space and time, are hydraulic conductivity K (L/T) and specific storativity (1/L). The complexity of the actual geometry of the fracture network, and the anisotropy of individual fractures is accommodated through the flow dimension, n, (Barker, 1988). When n=2 the Barker model simplifies to that of Theis (1935) representing purely radial flow. n=1 implies linear flow and the model is equivalent to that in Miller (1962). Finally, n=3 implies spherical flow. This concept of generalized radial flow allows the modelling of fractal behavior (e.g., n between 1 and 2; Bangoy et al., 1992).

In Barker's model, all parameters are strictly homogeneous, both in space and time. The limitation about spatial heterogeneity has been circumvented for example by nSIGHTS (2011) and Rafini and Larocque (2009). However, none of these works can cope with the temporal and spatial variability of flow dimension, which precludes Barkers analytical solution for its application in the context of the stimulation of geothermal boreholes.

To that end, the nSIGHTS code has been updated. The optimization algorithm was improved to the more robust "Global Optimum Determination by Linking and Interchanging Kindred Evaluators" (GODLIKE) algorithm developed by Oldenhuis (2016). The discretization is 1D radial and composed of 200 logarithmically spaced nodes. Each node has a value of n [-], permeability (K [m/s]), and specific storage (S [1/m]). The end node has a Dirichlet boundary condition (no-flow boundary) at 2500 m from the borehole. Aquifer thickness is 1 m, and borehole radius is 0.118 [m]. Borehole storage effect is taken into account with a constant borehole volume and water compressibility of 129.95 [m^3] and 4.4E-10 [1/Pa], respectively (Alcolea and Meier, 2011). The initial reservoir parameters were optimized from the pre-stimulation injection tests which yielded n_f=1.57, K_f=3.2E-7, S_f=3.7E-4. For simplicity, these parameters are assumed homogeneous within the unstimulated reservoir.

The code is designed to work on 2 main steps. The first step identifies when potential changes in hydraulic parameters may occur and splits the pressure curve into segments between the corresponding timestamps. The second stage optimizes model parameters for each split segment. These steps are described in detail below:

3.1 Step 1: Automatic detection of timesteps of parameter changes

To that end, the amplitude of the pressure variations analysed first (i.e., diagnostic plot analysis; Renard et. al, 2009) and the largest peaks above a certain threshold (0.04 MPa in this work) are selected (Figure 6a). During the injection phase, these usually coincide in time with seismic events. If they do not, the timestamp of the pressure variation can be associated with an unlocated and/or aseismic

event. Regardless of the character, we will refer here to these events as “Type I”, leading to identifiable pressure variations. All other events are tagged as “Type II”.

Type I events are usually located close to the wellbore. This is revealed by the large perturbation they cause in the pressure curve. Since the location accuracy (±70 m; Dyer et. al, 2010) is often larger than the distance between the located event and the inflow point, all of them are centred at the borehole. Instead, Type II events are either of low magnitude occurring at very early time near the borehole, or, occur farther away at late times as the stimulation progresses. As such, they do not play an important role in the pressure variation at the inflow. Regardless of event type, the source radius is calculated using the penny-shape model (Eshelby, 1957; Hanks and Kanamori, 1979) using the stress-drop catalogue calculated by Goertz-Allman (2011).

The section of transient curve between two Type 1 events, and all Type II events within it, defines a time interval where model parameters will be calibrated (Figure 6a).

3.2 Step 2: Calibration of model parameters

At the beginning of each time sequence there is a Type I event, and the goal is to update the K(r), S(r), and n(r) profiles of the previous time sequence (Figure 6b). Consequently, four parameters will be optimized: a constant T, S, n within the interval [0 and r*] Figure 6c). The parameters are optimized using the GODLIKE algorithm with the default options.

To avoid minima outside sensible parameter values, a set of bounds based on prior information is given for K, S, n. For the injection phase (t < 137.7 h) the lower bounds for *n, K,* and *S* are 1 [-], K_f [m/s], and 5E-6 [1/m]; while the upper bounds are 2 [-], 3E-4 [m/s], and 5E-5 [1/m]. The upper bound of *K* and the bounds for *S* are taken from the calculated values of Alcolea and Meier (2011). The bounds for *S* were constrained within 1 order of magnitude to prevent the formation of no-flow or partial boundaries within the reservoir. The shut-in and bleed-off phase (t > 137.7 h) have as maximum *K* corresponding to largest value optimized during the injection phase, and a maximum *S* of S_f. The bounds for the optimized r* are based on the source radius of Type I events calculated in the previous step. The absolute localization accuracy (±70 m) added to the maximum radius found among all Type I events (58.5 m) is considered as the maximum possible radius a seismic event can have (i.e. 128.5 m).

Type II events contained within each time sequence cannot be incorporated into a minimization function. Instead the K(r), S(r), and n(r) profiles are corrected proportionally to the event source (Figure 6d). The amount of increase to the profiles calculated for Type I events correlates with the source area of the event, i.e. the larger the event is and the closer to the borehole it is, the larger the perturbation. The details are out of the scope of this paper and will be published elsewhere.

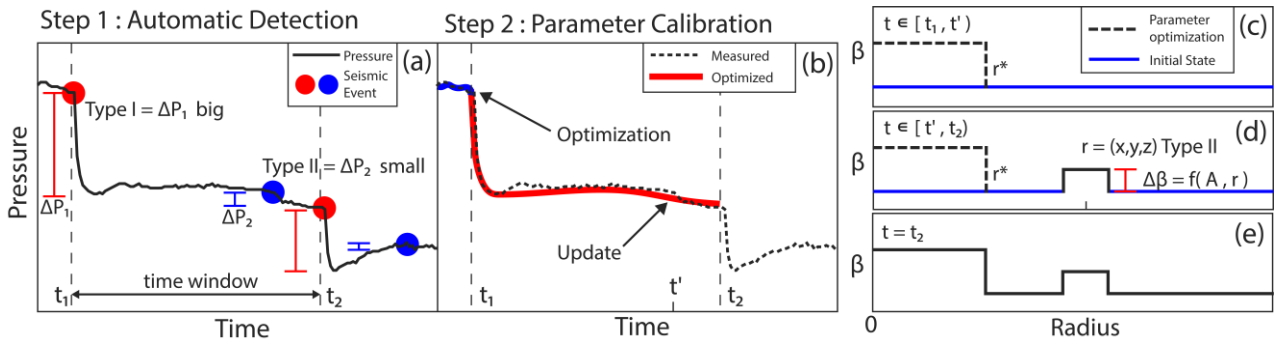

Figure 6: Schematic algorithm calculation routine on an idealized time segment. a) Step 1 schematic. Automatic detection of Type I and II events and creation of a time sequence between two Type I events, here marked as t1 and t2, b) Step 2 schematic: optimization of parameter profiles and correction for each Type II event. c), d) Schema of the changes done on the parameter (here named β) profile within each iteration of the optimizer, and e) the end result should it present good fit. Dotted lines are optimized parameters, while the bold lines are fixed.

4. RESULTS

The goal of the simulation was to model the Basel EGS which is consistent with observations. The fit of the observed pressure curve is very good, (Figure 7a) and the fit with seismic event frequency for the injection phase is accurate (Figure 7b). The bleed-off phase is consistent with the assumption that areas of higher seismic event frequency should have a higher pressure, and a drop-in seismicity should be concurrent to a drop-in pressure.

The first Type I event of the injection phase drops *n* to 1.4 which then rapidly increases to 1.85 during the early time (t < 16.6 h). K also increases during the early and mid-time (t < 69.4 h) by two orders of magnitude reaching a plateau at ≈5E-5 [m/s]. During the late time period (69.4 h to shut-in) both n and K remain stable until the shut-in. As expected, S remains between the maximum and minimum brackets of 5E-5 [1/m] and 5E-6 [1/m] through the injection phase. (Figure 8b)

The recovery is characterized by two events. First, a sudden drop in *K* during the shut-in followed by a sudden increase at the bleed-off. Second, a steady decrease in *n* from 1.98 to 1.41 during the bleed-off phase (Figure 8b), and an increase of S to pre-stimulated values. The parameter update of Type II events yielded a good fit with the radial extent of the seismic cloud (Figure 8a). More detailed results for all parameter updates can be seen spatiotemporally in Figure 9.

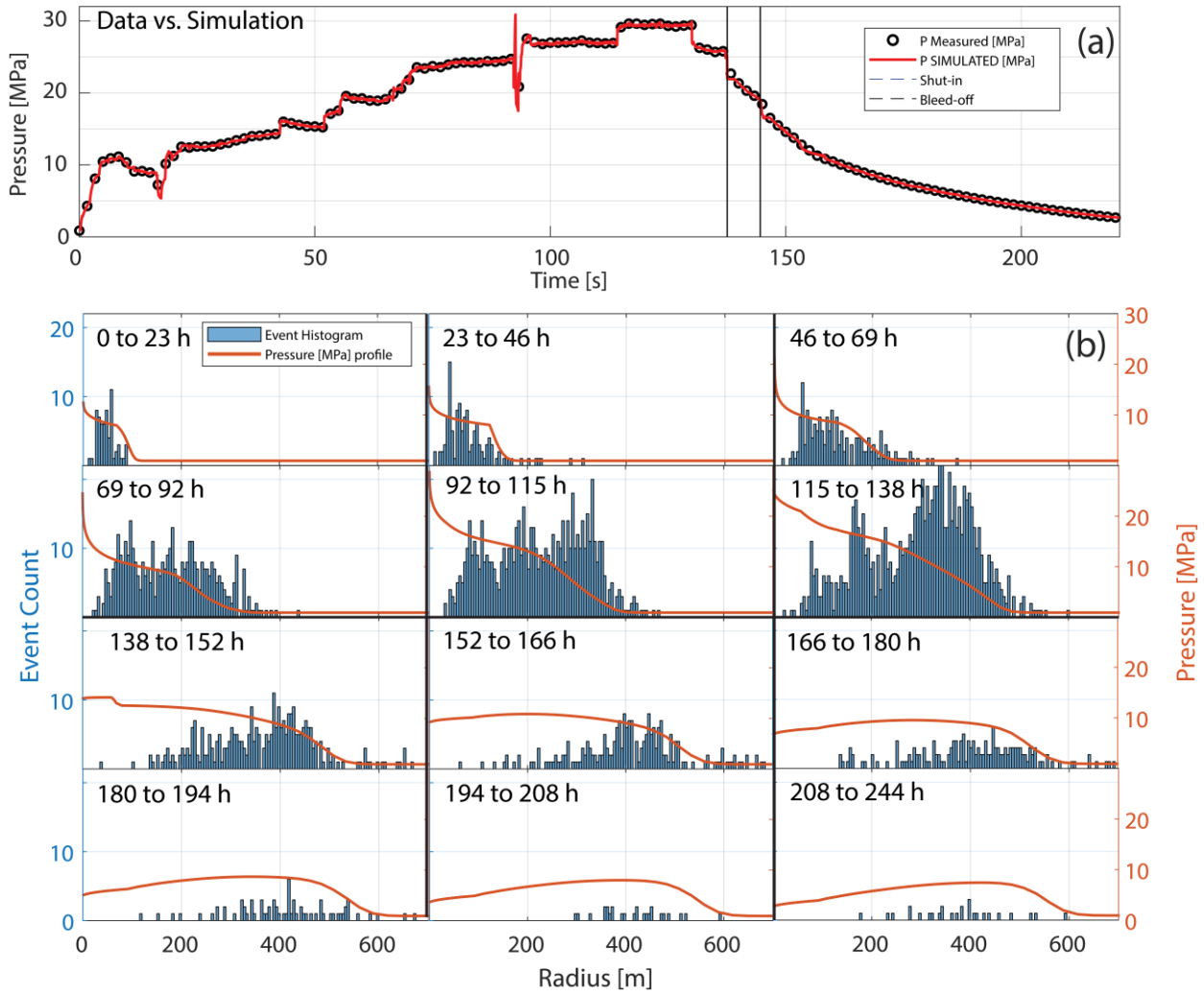

Figure 7: Parameter calibration goodness fit. a) Pressure transient curve minimized by the optimizer. The two black lines denote the shut-in and bleed-off. b) Radial extent of the pressure profile compared to frequency of events for 12 periods of the stimulation. The six above (t < 138 h) correspond to the injection, while the six bellow (t > 138 h) are the recovery phase.

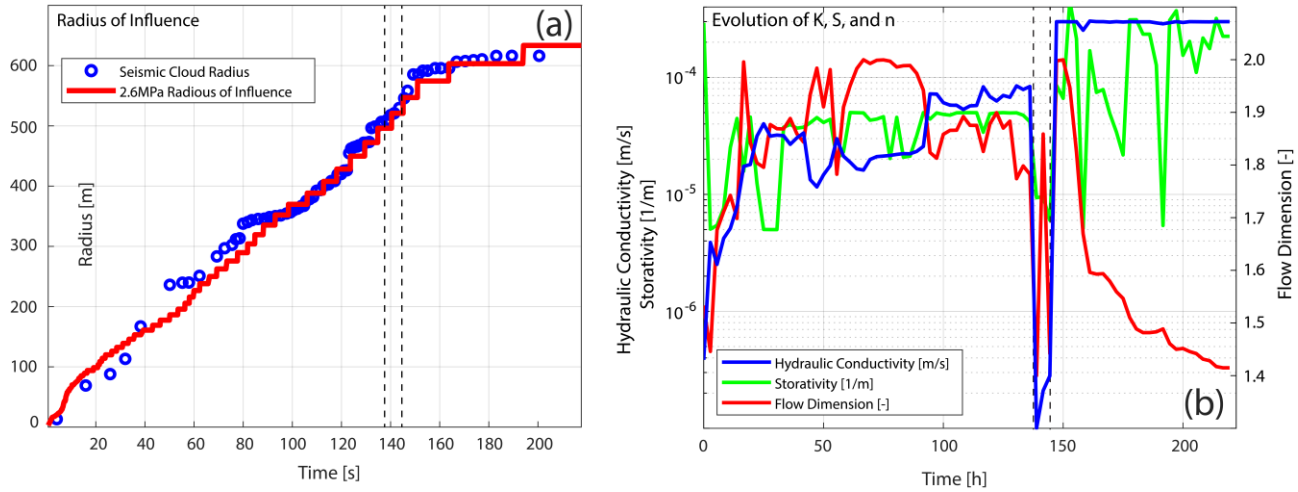

Figure 8: Parameter optimization results. a) Type II event update goodness fit quantification. The simulated pressure profile was compared to the average between the convex and concave hull (blue circles). The dotted lines denote the shut-in and bleed-off. b) Parameter calibration for Type I events.

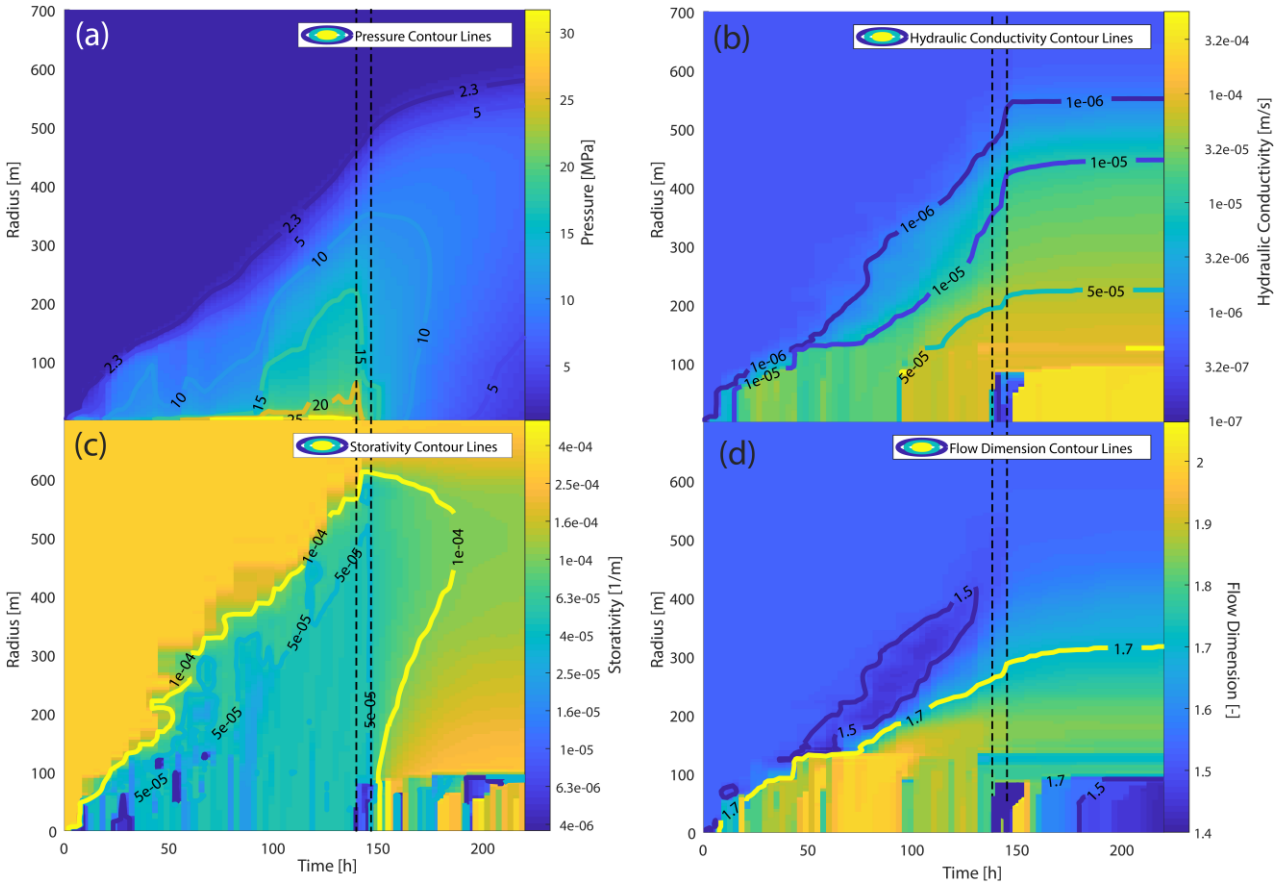

Figure 9: Spaciotemporal evolution of parameter profiles. Doted lines denote shut-in and bleed-off. a) Pressure profile, b) hydraulic conductivity (K), c) storativity (S) and finally, d) flow dimension (n).

5. CONCLUSION

The evolution of *K* during the stimulation is consistent with the conceptual model in which early and mid-times are dominated by improvement in *K*, while late times are dominated by a *K* plateau and reservoir expansion. The values for K are in good agreement with previous hydraulic models that also detected a plateau at 7E-5 [m/s] (Alcolea and Meier 2011). Conversely, storativity shows conflicting results. S should increase during the injection phase (Rutqvist et al., 1998) but instead it decreases. The optimizer was set to inverse the S, but the goodness fit with both borehole pressure and the seismic cloud decreased.

The shut-in phase shows an abrupt decrease in K, which could be the effects of fracture compliance. Other authors suggest that it is caused by a rapid collapse of the turbulent pressure profile within the fractures (Ortiz et al, 2011). In either case, the results for the shut-in phase are speculative at best.

A decrease in *K* was also expected during the bleed-off but surprisingly there was a decrease in *n* from 1.98 to 1.41, which implies a transition from radial flow to linear flow. Other solutions were attempted by forcing the optimizer to lower K, maintain n constant, and allow S to vary as far as necessary. No solution within sensible parameter values was found. This result suggests the existence of preferential flow paths within the reservoir or fractures, which had a marginal presence during the injection phase with an *n* slightly lower than 2. We hypothesize that pressure release causes the fractures to close and therefore causes the backflow to pass preferentially through major flow paths (or “canals”). Also, since *K* does not decrease, it strongly suggests that these preferential flow paths are the major contributors to permeability.

Because of the simplicity of this model, the simulation can be performed in 30 minutes on a regular desk top machine, which opens the possibility of using the model in real-time assessments of future EGS projects.

6. CONCLUSION

We analyse the hydraulic effects that seismic events have on borehole pressure, notably the sharp pressure variations which are associated with the timestamp of seismic events. Then, we show that the amplitude of pressure variations depends on the event magnitude and the proximity to the well. Further, we show that the stimulation is characterized by two regimes, one in which hydraulic properties are improved, and a second one where the reservoir expands. To reproduce the observations, we construct a 1D radial model that incorporates spaciotemporal variations of flow dimension, hydraulic conductivity and storativity. The results show that the stimulation reached a plateau in hydraulic conductivity during injection and that the recovery after shut-in and backflow shows a decrease in flow dimension linked to preferential flow in “canals” that are possibly formed as fractures apertures decrease in the vicinity of the well because of pressure reduction.

We conclude that the borehole pressure data coupled with the seismic catalogue can be used to approximate the evolution of the stimulation process. Future projects should consider investing heavily on state-of-the-art seismic arrays and piezometers to further improve our understanding of an EGS reservoir.

Acknowledgments

This work was supported by the Swiss State Secretariat for Education, Research and Innovation (SERI) under contract number 15-0316-1. The opinions expressed and arguments employed herein do not necessarily reflect the official views of the Swiss Government. We thank Andrés Alcolea Rodriguez for the quality control of the code and the editorial supervision of the paper.

REFERENCES

Alcolea, A., and Meier, P.: Re-evaluation of hydraulic tests in borehole BS-1 (Report No. v6), (2011), Zurich, Geo-Energie Suisse AG.

Barker, J.A.: A generalized radial flow model for hydraulic tests in fractured rock, *Water Resources Research,* **24.10**, (1988): 1796-1804.

Bangoy, L.M., et al.: A new method of characterizing fissured media by pumping tests with observation wells, *Journal of Hydrology,* **138.1-2**, (1992): 77-88.

Birsoy, Y.K., and Summers, W.K.: Determination of aquifer parameters from step tests and intermittent pumping data, *Groundwater,* **18.2**, (1980): 137-146.

Deichmann, N., Kraft, T., and Evans, K.F.: Identification of faults activated during the stimulation of the Basel geothermal project from cluster analysis and focal mechanisms of the larger magnitude events, *Geothermics,* **52**, (2014): 84-97.

Dyer, B.C., et al.: Application of microseismic multiplet analysis to the Basel geothermal reservoir stimulation events, *Geophysical Prospecting,* **58.5**, (2010): 791-807.

Eshelby, J.D.: The determination of the elastic field of an ellipsoidal inclusion, and related problems, *Proceedings of the Royal Society of London. Series A. Mathematical and Physical Sciences,* **241.1226**, (1957): 376-396.

Goertz-Allmann, B.P., Goertz, A., and Wiemer, S.: Stress drop variations of induced earthquakes at the Basel geothermal site, *Geophysical Research Letters,* **38.9**, (2011).

Häring, M.O., Schanz, U., Ladner, F., and Dyer, B.C.: Characterisation of the Basel 1 enhanced geothermal system, *Geothermics,* **37.5**, (2008): 469-495.

Hanks, T.C., and Kanamori, H.: A moment magnitude scale, *Journal of Geophysical Research: Solid Earth,* **84.B5**, (1979): 2348-2350.

Jalali, M, et al.: Transmissivity Changes and Microseismicity Induced by Small-Scale Hydraulic Fracturing Tests in Crystalline Rock, *Geophysical Research Letters,* **45.5**, (2018): 2265-2273.

Miller, F.G.: Theory of unsteady-state influx of water in linear reservoirs, *J. Inst. Pet,* **48.467**, (1962): 365-379.

Mukuhira, Y., et al.: Pore pressure behavior at the shut-in phase and causality of large induced seismicity at Basel, Switzerland, *Journal of Geophysical Research: Solid Earth,* **122.1,** (2017): 411-435.

nSIGHTS, Geofirma Engineering Ltd., and INTERA Inc.: nSIGHTS User Manual, (2011), Version 2.50

Oldenhuis, R.: Global Optimum Determination by Linking and Interchanging Kindred Evaluators, (2016), version 1.4.0.0. https://www.mathworks.com/matlabcentral/fileexchange/24838-godlike-a-robust-single-multi-objective-optimizer

Ortiz R, A.E., Renner, J., and Jung, R.: Hydromechanical analyses of the hydraulic stimulation of borehole Basel 1, *Geophysical Journal International,* **185.3**, (2011): 1266-1287.

Rafini, S., and Larocque, M.: Insights from numerical modeling on the hydrodynamics of non-radial flow in faulted media, *Advances in water resources,* **32.8**, (2009): 1170-1179.

Renard P., Glenz D., and Mejias M.: Understanding diagnostic plots for well-test interpretation*, Hydrogeology Journal*, **17.3**, (2009): 589-600.

Rutqvist, J., Noorishad, J., Tsang, C. F., and Stephansson, O.: Determination of fracture storativity in hard rocks using high-pressure injection testing, *Water Resources Research*, (1998), **34.10**, 2551-2560.

Serbeto, F. and Meier, P.M.: Good Agreement of Fracture Sets Detected by Acoustic Televiewer with Fracture Clusters Revealed by Microseismicity Within the Basel EGS Reservoir, *Proceedings* World Geothermal Congress, Iceland, 2020. Manuscript submitted for publication (copy on file with author).

Terakawa, T., Miller, S.A., and Deichmann, N.: High fluid pressure and triggered earthquakes in the enhanced geothermal system in Basel, Switzerland, *Journal of Geophysical Research: Solid Earth,* **117.B7**, (2012).

Terakawa, T.: Evolution of pore fluid pressures in a stimulated geothermal reservoir inferred from earthquake focal mechanisms, *Geophysical Research Letters,* **41.21**, (2014): 7468-7476.

Theis, C.V.: The relation between the lowering of the piezometric surface and the rate and duration of discharge of a well using ground-water storage, *Eos, Transactions American Geophysical Union,* **16.2**, (1935): 519-524.

Ziegler, M., Valley, B., and Evans, K.F.: Characterization of natural fractures and fracture zones of the Basel EGS reservoir inferred from geophysical logging of the Basel-1 well, Proceedings *World Geothermal Congress Melbourne, Australia*, 2015.